2020

New insights into the corrosion behaviour of medium manganese steel exposed to a NaCl solution spray

Guanqiao Su
University of Wollongong, guan@uow.edu.au

Xiuhua Gao

Mingshuai Huo
University of Wollongong, mh317@uowmail.edu.au

Haibo Xie
University of Wollongong, xie@uow.edu.au

Linxiu Du

See next page for additional authors

New insights into the corrosion behaviour of medium manganese steel exposed to a NaCl solution spray

Abstract

© 2020 Elsevier Ltd A medium manganese steel with an appropriate concentration of chromium (0.8 wt.%) and other anti-corrosion elements (0.3Ni-0.3Cu-0.2Mo in wt.%) was studied with the aim of further characterizing the corrosion feature (via corrosion kinetics, XRD, SEM, EPMA and XPS) exposed to a NaCl solution spray. The results reveal that the increased Mn and Cr contents in medium manganese steel change the corrosion performance at different stages. The formation of the initial corrosion product β-FeO(OH) and high cationic fraction of Mn ions directly cause the high corrosion rate. The higher Cr content contributed to providing better protection when the barrier formed.

Disciplines

Engineering | Science and Technology Studies

Publication Details

Su, G., Gao, X., Huo, M., Xie, H., Du, L., Xu, J. & Jiang, Z. (2020). New insights into the corrosion behaviour of medium manganese steel exposed to a NaCl solution spray. Construction and Building Materials, 261

Authors

Guanqiao Su, Xiuhua Gao, Mingshuai Huo, Haibo Xie, Linxiu Du, Jianzhong Xu, and Zhengyi Jiang

New insights into the corrosion behaviour of medium manganese steel exposed to a NaCl solution spray

Guanqiao Su[a], Xiuhua Gao[b,*], Mingshuai Huo[a], Haibo Xie[a], Linxiu Du[b], Jianzhong Xu[b], Zhengyi Jiang[a,*]

[a] School of Mechanical, Materials, Mechatronic and Biomedical Engineering, University of Wollongong, NSW 2522, Australia

[b] State Key Laboratory of Rolling and Automation, Northeastern University, Shenyang 110819, China

[*]Corresponding authors, E-mail addresses: gaoxiuhua@126.com (X. Gao), jiang@uow.edu.au (Z. Jiang)

ABSTRACT: A medium manganese steel with a high concentration of chromium (0.8 wt.%) and other anti-corrosion elements (0.3Ni-0.3Cu-0.2Mo in wt.%) was studied with the aim of further characterizing the corrosion feature (via corrosion kinetics, XRD, SEM, EPMA and XPS) exposed to a NaCl solution spray. The results reveal that the increased Mn and Cr contents in medium Mn steel change the corrosion performance at different stages. The formation of the initial corrosion product β-FeO(OH) and high cationic fraction of Mn ions directly cause the high corrosion rate. The higher Cr content contributed to providing better protection when the barrier formed.

KEYWORDS: Medium Mn Steel; EPMA; Weight loss; XPS; Corrosion

1. INTRODUCTION

During the last two decades, due to the shortage of land resources and energy exhaustion, the marine industry has been faced with increasing pressure from environmental groups to reduce the service life of facilities and increase oil leakage [1, 2]. On one hand, marine structures must

possess superior and comprehensive mechanical properties, on the other hand, the cost and the service life of raw materials are considered to ensure their products with economic usage and reliability. Medium Mn steels (containing 3-10 wt.% Mn) with a thickness specification of 30~80 mm were proposed and declared to rival HSLA-100 steel (0.005C-1.2Mn-2.1Cu-0.6Cr-0.6Mo-3.5Ni-0.05Nb in wt.%) because of their excellent homogeneous microstructures, superior mechanical properties, and good balance of strength and low-temperature toughness, and the medium Mn steels can reduce the cost for additions of alloying elements [3]. A suitable quenching and intercritical tempering (Q&T) process allows high-strength ferrite/martensite and stable reversed austenite structures to be obtained by increasing the concentration of C and Mn in austenite during the partitioning treatment [4, 5]. Nevertheless, low levels of anti-corrosion elements and high Mn concentrations result in a more unique corrosion performance relative to that of the low alloy steel.

Recently, attempts have been made to clarify the influence of Mn addition on the corrosion behaviour of medium/high Mn steel by performing accelerated corrosion testing and electrochemical testing [6-8]. Fajardo et al. [6] reported that the corrosion rate increases as the Mn content increases in high Mn steel, and the enrichment of Mn oxides in the corrosion product was found to increase as the Mn content increased, accompanied by a decrease in the Fe oxide content. Therefore, the addition of Mn increases the corrosion susceptibility and reduces the corrosion resistance. Moon et al. [7] used an electrochemical method to study the effect of the Mn content on the corrosion characteristics of high Mn TWIP steel, it was suggested that the corrosion resistance of high Mn steel can be reduced by producing a high density of deformation twins and large surface energy grain boundaries. In the case of the medium Mn steel, manganese compounds form in the corrosion products in the simulated marine splash zone environments but do not form in the simulated marine immersion zones [8]. These formed corrosion products can deteriorate the protective ability of the medium Mn steels because they have a higher corrosion current density and lower total impedance value. However, the effect of Mn on the corrosion behaviour of the medium Mn steel in the neutral salt spray condition has not been elucidated.

In the current work, the corrosion behaviour of the Q&T medium Mn steel containing four low level anti-corrosion elements (Ni, Cu, Mo and Cr) exposed to a NaCl solution spray was studied

by evaluating the corrosion kinetics curves, corrosion phases, surface and cross-sectional morphologies and elemental distributions, as well as the valence state. These new insights into the corrosion behaviour of the medium Mn steel may provide the valuable data necessary to develop a medium Mn steel with relevant corrosion protection. Furthermore, the effect of increasing the concentration of Mn (5.9 wt.%) and Cr (0.8 wt.%) in the corrosion process of the medium Mn steel has been studied and compared with that of the medium Mn steel described in the previous study and exposed to the same environment [9].

2. EXPERIMENTS

2.1 Materials

The chemical compositions of the experimental medium manganese steel are listed in Table 1. The medium manganese steel was melted using a vacuum furnace, cast and forged into a billet with an ~140 mm thickness. The hot rolling and heat treatment process are illustrated in Fig. 1. The billets were homogenized at 1,200 °C for 2 h and then hot rolled to 30 mm via eleven passes. The start and finish temperatures during the hot rolling process were 960 °C and 900 °C, respectively. The phase transformation temperatures were measured using a DIL 805 A/D dilatometer in a nitrogen atmosphere. Test coupons with dimensions of 10 × 4 × 2 mm^3 were cut from the directly water-quenched steel plate. The coupons were heated at a heating rate of 0.1 °C/s to 1,000 °C to simulate the slow heating process and were then quenched to room temperature at 20 °C/s. The critical temperatures M_f, M_s, Ac_1 and Ac_3 were measured by the dilatometer, which were 258 °C, 377 °C, 594 °C and 796 °C, respectively. Based on the phase transformation temperature, the directly water-quenched plates were reheated for 50 min to an intercritical tempering temperature of 650 °C. Then, the plates were air-cooled to room temperature.

2.2 Neutral salt spray tests

The neutral salt spray tests were performed in a salt spray test chamber (YWX/Q-020; Beijing Yashilin Testing Equipment Co., Ltd.; Beijing, China) for 24 h, 72 h, 168 h, 288 h 432 h and 600 h according to DIN EN ISO 9227 [10]. The test solution was a 5 wt.% NaCl solution. Coupons with two sizes of 40 mm × 40 mm × 4 mm and 10 mm × 10 mm × 4 mm were cut from the tested medium manganese steel for corrosion rate calculation and corrosion products analysis. A burnishing process was carried out of the coupons surfaces using 240, 400, 600, 800,

and 1200 grit silicon carbide sand papers. Grease and dust on the coupons were removed with acetone and alcohol using an ultrasonic cleaner, and the coupons were dried with clean air at room temperature. In order that only one larger side encounters corrosion, the rims and backsides of the coupons were sealed with an anti-salt fog varnish (PLASTIK 70, Kontakt Chemie) [11]. Five replicate coupons were used for each corrosion cycle. The test conditions were as follows: the tested temperature, pH value and deposition rate of the NaCl solution were 35 °C, 6.5, and 1.6 ml/h, respectively.

The description of the corrosion kinetics is based on the weight loss of the coupon after each corrosion cycle. First, corroded coupons were carefully rinsed and dried. The anti-salt fog varnish on the coupon was removed by a hard plastic piece. The corrosion products were visually removed after the corroded areas were carefully cleaned by an electrochemical treatment. Hexamethylenetetramine (10 g) and 37 (vol) % hydrochloric acid (100 mL) were dissolved in 1,000 mL distilled water. This procedure did not result in any further electrochemical reaction of the steel matrix [12].

2.3 Morphology observation and corrosion products analysis

Transmission electron microscopy (TEM; FEI Tecnai G^2F20) was used to observe the microstructure of the medium manganese steel. The mechanical properties of the medium manganese steel were evaluated using a Shimadzu AG-X universal tensile machine with a crosshead speed of 3 mm/min and an Instron Dynatup 9200 series drop weight impact tester. After the salt spray test, the surface and cross-sectional morphologies of the corrosion products were studied using a field emission scanning electron microscope (SEM; ZEISS ULTRA55) and a JEOL-8530F electron probe micro-analyser (EPMA) equipped with an energy dispersive X-ray spectrometer (EDX). Furthermore, a D/max 2400 X-ray diffraction (XRD) system equipped with CuKα radiation (λ = 0.154 nm) was used to study the phases and corrosion product composition of the tested medium manganese steel. XRD data were collected from 40° to 100° and 10° to 70°. In addition, X-ray photoelectron spectroscopy (XPS; ESCALAB 250) was carried out to identify the valence state of the elements in the formed corrosion products.

3. RESULTS

3.1 Microstructure and mechanical properties

It is well known that reversed austenite can form in medium manganese steels via an

intercritical annealing/tempering treatment [13, 14]. Reversed austenite plays an important role in the comprehensive properties of steels [15-17]. After intercritical tempering was performed at 650 °C for 50 min, the microstructure of the tested medium manganese steel consisted of lath-like martensite and oval-like reversed austenite (as shown in Fig. 2a). The reversed austenite was distributed along the boundary of the lath-like martensite, which was confirmed by the dark field micrograph and selected area electron diffraction (SAED) pattern shown in Fig. 2b and its inset map. The phase composition was determined based on the XRD pattern shown in Fig. 2c. The volume fraction of the reversed austenite was quantified by a calculation reported by Hu et al. [18] using the integrated intensities of (200)α, (211)α, (200)γ, (220)γ and (311)γ. Approximately twenty-five percent of austenite was obtained after intercritical tempering.

By using the EDX results obtained from TEM, the main chemical composition of Mn, Ni and Cr was 8.85Mn-0.51Ni-0.89Cr (wt.%) in the reversed austenite and 4.51Mn-0.44Ni-0.57Cr (wt.%) in the martensite (Fig. 2d). The EDX results indicated that the distribution of Mn and Cr significantly increased in the austenite during the intercritical tempering process, along with the reverse transformation of austenite. Therefore, the partitioning of Mn and Cr during intercritical annealing was consistent with that expected from the tested medium manganese steel. Elemental Mn can provide a strong interfacial segregation effect and can stabilize austenite, while the anti-corrosion effects of elemental Cr offset the adverse effect of Mn to balance the corrosion process [9].

A good combination of strength and toughness was obtained in the medium manganese steel after intercritical tempering. The mechanical properties are presented in Figs. 3a and 3b, the yield and tensile strength of the tested steel were 710 MPa and 842 MPa, respectively, and the Charpy absorbed energy values at 0 °C, -20 °C, -40 °C and -60 °C were 211 J, 192 J, 143 J and 105 J, respectively. It is reasonable to infer that the transformation-induced plasticity (TRIP) effect induced by the reversed austenite can reinforce the strength and toughness under the stress loading condition.

3.2 Corrosion kinetics and corrosion product

Based on the standard ASTM G1-03 [19], the weight changes (Δm) of the medium Mn steels were determined based on the differences between the original weight of the coupon and the

weight after removing the corrosion products. The corrosion kinetics curve (Fig. 4) was characterized by determining the value of the average corrosion rate. The average corrosion rate (ACR, mm·y^{-1}) was calculated according to Eq. (1).

$$ACR = \frac{87{,}600\Delta m}{t\rho S} \quad (1)$$

where Δm is the weight change in g, t is the corrosion time in hours, ρ is the physical density of the tested steel, and S is the area of the largest surface of the coupon in cm^2.

The average corrosion rate obtained for the tested medium Mn steel for different bathing times in the neutral salt spray condition is connected to the plot of the corrosion kinetics curve. The corrosion curve (see Fig. 4) trends continuously to decline. The initial stage involves the average corrosion rates sharply reducing from 24 h to 288 h. However, the average corrosion rate slightly decreases after the next bathing time node. Then, the corrosion curve from 432 h to 600 h is stable. The relative stable value of the corrosion rate in the neutral salt spray is 0.77 ± 0.02 mm·y^{-1}.

The evolution of the corrosion products directly indicates the change in the average corrosion rate [20]. Fig. 5 indicates that the main surface corrosion products are lepidocrocite, γ-FeO(OH), iron oxide, Fe_2O_3 or Fe_3O_4, manganese oxide, Mn_2O_3 or Mn_3O_4, and small amounts of goethite, α-FeO(OH), and akageneite, β-FeO(OH). The XRD patterns (Figs. 5a and 5b) reveal that FeO(OH) actually presents as three polymorphs (γ-FeO(OH), α-FeO(OH) and β-FeO(OH)). However, β-FeO(OH) was not observed in the corrosion products when the corrosion time was longer than 168 h. As a result, the average corrosion rate of the tested medium Mn steel is constantly high in the initial corrosion stage. Furthermore, the sharp fluctuation of the diffraction intensities of γ-FeO(OH) with increasing corrosion times is caused by the reduction of the reaction of γ-FeO(OH) during the corrosion process. As the main corrosion phase, γ-FeO(OH) is deposited in the corrosion product, and upon thickening of the corrosion product, these γ-FeO(OH) can also regenerate as the corrosion time increased [21]. Additionally, the critical peak of more stable corrosion products α-FeO(OH) became intense after corrosion testing times of 432 h and 600 h. As mentioned above, it can be seen that the variation trend of FeO(OH) in the corrosion products corresponds to the corrosion kinetics curve and synchronously changes with increasing corrosion times. Besides, the content of iron oxide and

manganese oxide are changed in the surface corrosion products of the tested medium Mn steel. The phase content of the iron oxides reaches its maximum value after 72 h of corrosion testing time. Similarly, the peak intensity corresponding to the manganese oxides starts to decrease and become more stable after the initial two corrosion durations.

3.3 Surface and cross-sectional observations

The surface morphology of the corrosion products, specifically, the characteristic morphology and compactness, can be used to study the corrosion process [22, 23]. The crevices in the initial corrosion products (Figs. 6a and 6b) mean that the salt spray deposition process occurs by local condensation. The excessive concentration of chloride ions in the localized areas causes cloud-like β-FeO(OH) to form in the initial corrosion products. Globular and lamellar formations exist in most areas on the surface. These morphologies corresponding to γ-FeO(OH) are mentioned by other publications [24-26]. As γ-FeO(OH) forms, the corrosion products become more compact. In addition, some needles or whiskers typical of α-FeO(OH) appear around the periphery of γ-FeO(OH) [27-29]. With increasing corrosion testing time, the FeO(OH) morphology presents with the main phases and corresponds to a mixture of globular γ-FeO(OH) and α-FeO(OH) needles/whiskers, where the latter forms from the transformation of the former, which causes the compactness of the corrosion product to gradually increase (Figs. 6c-6e). During the final corrosion, the surface morphology did not significantly transform (Fig. 6f). The innermost surface characterized by exfoliated formations was a blackish colour, possibly corresponding to magnetite, Fe_3O_4, which agrees with the XRD patterns (Fig. 5f). It seems to be confirmed that FeOOH is located on the outermost surface, and Fe_3O_4 mainly exists on the innermost surface.

Fig. 7 shows the cross-sectional morphologies of the corrosion products that formed on the tested medium Mn steel after its corrosion for different times in the neutral salt spray condition. The values on the red line and bottom marking in Fig. 7 are the maximum thickness values of the selected corrosion products and the loss in thickness of the steel matrix, respectively, which was calculated using the data of the average corrosion rate. A monolayer structure with a maximum thickness of 7.5 μm appears above the matrix after a corrosion testing time of 24 h (Fig. 7a). The initial corrosion product presents with an uncompacted state, is poorly protected against corrosive media and has a high average corrosion rate. After a corrosion testing time of

72 h, the maximum thickness of the corrosion product is 31.3 μm, and the compactness increases. Furthermore, cracks appear in the corrosion products near the side of the steel matrix (Fig. 7b). As the corrosion testing time increases to 288 h, the maximum thickness of the corrosion product is 83.2 μm, and the compactness of the corrosion product becomes better (Fig. 7c). Figs. 7d-7f show that the maximum thickness of the corrosion product of the tested medium Mn steel does not significantly increase, and the structural continuity of the corrosion product is gradually improved, except that some changes in the structural characteristics of the outer film of the corrosion product have occurred. The gradual increase in the compactness of the outer film has improved the protective ability of the corrosion products, to some extent. Additionally, the cracks probably affect the protective ability of corrosion product even if the corrosion product is dense. Longitudinal cracks parallel to the matrix and transverse crack of the vertical matrix appear in the corrosion products after a corrosion time of 288 h. These cracks provide a channel for the penetration of chloride and oxygen ions, which causes an accelerated corrosion phenomenon to occur.

3.4 Elemental distribution and valence state

Fig. 8 shows the chemical composition maps (Fe, Mn, Cu, Ni, Mo and Cr) of the tested medium Mn steel corrosion products, which were obtained by an electron probe micro-analyser (EPMA) after all the corrosion cycles. It is evident that the corrosion film contains regions that are depleted and enriched in alloying elements and that the degrees of enrichment and depletion change somewhat as the corrosion time increases. The enriched regions of elemental Fe and Mn are significant. However, the evolution of enrichment with the increase of corrosion testing time occurs with different changes. In the initial corrosion testing time stage (24 h), the corrosion products are minimally enriched in Fe and Mn. In contrast to the continuous enrichment of elemental Fe, less elemental Mn enrichment is observed after the last three corrosion cycles, and a depletion phenomenon appears relative to the concentration of elemental Mn in the matrix. In addition, except for Ni, which is apparently enriched in the initial stage of the corrosion process, the other elements (Cu, Mo and Cr) are enriched in the gap between the matrix and corrosion products during the last three cycles. Among Cu, Mo and Cr enrichment, elemental Cr enrichment is the most significant, and the enriched region corresponds to the region depleted in elemental Mn in the corrosion products.

The high-resolution XPS spectra of the Fe 2p, Mn 2p and Cr 2p survey scans of the tested medium Mn steel after corrosion testing times of 168 h and 432 h are shown in Fig. 9. The survey spectra show five peaks assigned to O 1s, C1s, Fe 2p, Mn 2p and Cr 2p at the two different corrosion testing times. A small amount of Cr is detected whereas other elements are not observable due to low contents in tested steel. The peaks indicate that Fe and Mn play essential roles in the corrosion behaviour evolution, while the surface of the medium Mn steel was shown to be severely oxidized based on the apparent O 1s peak. The main composition of the corrosion product can be observed from the Fe 2p and Mn 2p XPS spectra (Figs. 10a and 10b). After a corrosion testing time of 168 h, it is found that the peaks at 711.4 eV and 724.6 eV from the Fe 2p spectra are attributed to Fe $2p_{3/2}$ and Fe $2p_{1/2}$, which provides clear evidence of the existence of Fe(III) in the corrosion product [30]. The deconvoluted Fe 2p spectra also show two peaks attributed to an oxide of Fe(II) at 709.8 eV and an oxyhydroxide of Fe(III) (FeOOH) at 713.5 eV [31, 32]. When the corrosion testing time is increased to 432 h, the Fe 2p spectrum contains two deconvoluted peaks at 710.6 eV and 724.1 eV, which correspond to Fe $2p_{3/2}$ and Fe $2p_{1/2}$, respectively, confirming the existence of Fe_3O_4 in the corrosion product [33]. At the same time, the deconvoluted peak at 713.5 eV in the Fe $2p_{3/2}$ spectrum indicates that FeOOH is still a primary compound in the corrosion product. Fig. 10b presents the deconvoluted Mn 2p spectrum obtained at the same corrosion testing time as the Fe 2p spectrum. At a corrosion testing time of 168 h, as seen in the fitted Mn $2p_{3/2}$ spectrum, two kinds of Mn oxides are detected: MnO and MnO_2 (Mn $2p_{3/2}$ centred at 640.7 eV and 642.5 eV) [34, 35]. The satellite peak of Mn(II) at 645.4 eV is detected as well. However, after a corrosion testing time of 432 h, it is observed that the Mn 2p spectrum only shows two components assigned to Mn $2p_{3/2}$ at 643 eV and Mn $2p_{1/2}$ at 654.5 eV, indicating that the Mn oxides (Mn_2O_3, MnO_2 and Mn_3O_4) are combined together in the corrosion product [6, 34].

4. DISCUSSIONS

The calculated corrosion kinetics, surface and cross-sectional observations made by SEM and the composition and elemental analyses of the corrosion products performed by XRD, EPMA and XPS in the present work indicate that the corrosion process that occurs on the surface of medium Mn steel after the salt spray tests comprises two different stages, suggesting that the effects of the alloying element on corrosion performance during the corrosion test are different.

A high concentration of Mn can accelerate the corrosion of the medium Mn steel in a neutral chloride solution, which is attributable to the increase of the dissolution current densities [6]. Similarly, adding Mn to the medium manganese steel also accelerates the corrosion rate, and the results from the calculation and characterization show that manganese agglomerates in the corrosion products obtained during the first three cycles. According to the neutral salt spray corrosion test results described in this paper, the mechanism responsible for the effects of the alloying elements on the corrosion process of the medium Mn steel is shown in Fig. 11.

Previous studies have reported that anti-corrosion elements such as Cr, Mo, Cu and Ni have a synergistic effect on the corrosion behaviour of the medium Mn steel [9]. Anti-corrosion elements play different roles in the different corrosion stages of the medium Mn steel. As mentioned in section 3.4, the enrichment of elemental Ni and Cu in the corrosion product occurs twice during the early and late stages of corrosion, while the other elements, Mo and Cr, are only gradually enriched at the matrix/product interface during the later stages of corrosion. The roles of the anti-corrosion alloying elements during the corrosion process of the medium Mn steel were summarized in the schematic. Low Ni (0.3 wt%) was substituted with Fe(III)/Mn(IV) in the corrosion products, thereby adversely affecting the electrical properties of the corrosion products during the whole corrosion process, and the characteristics showed that varying Fe/Mn ion contents were uniformly distributed throughout the corrosion products, as shown in Fig. 8 [36, 37]. However, the preferential nucleation property of Cu at the initial stage of corrosion increases the corrosion resistance, and Cu also enriches the inner layer of the corrosion product during the second corrosion stage, enhancing the density, which is similar to the effect of Cr [37, 38]. In addition, the insoluble Mo oxide acts to reduce the cation permeability in the second corrosion stage [39].

The present results of the corrosion process observed in the neutral salt spray test relative to the previous parallel test result [9] shows that the final corrosion rate decreases in the medium Mn steel when the Cr content is increased from 0.4 to 0.8 wt.%, whereas the initial corrosion rate increases when the Mn content is increased from 5.6 to 5.9 wt.%. Note that in the previous parallel test results, the medium manganese steel contained comparatively lower Mn contents and lower Cr contents than the presently studied medium Mn steel, which is the main cause for the different corrosion rates. Another aspect to consider is the volume fraction of austenite in

the medium Mn steel tested in this study, approximately 25%, which is more than that in the previous studied steel [9]. The monolayer of corrosion products formed at the beginning of the corrosion process, where the corrosion process proceeds with the highest corrosion rate, essentially consists of Fe and Mn and also shares aspects of the elemental composition of the medium Mn steel, which is expected when the corrosion product has a low corrosion resistance and allows for the direct electrochemical reaction to occur due to β-FeO(OH), especially in environments with Cl^- ions and when excess Mn exists in the matrix [40]. Mn continues to oxidize until the enriched region of Cu, Mo and Cr forms at the matrix/product interface during stage one. Therefore, compared to previous studies, the higher Mn and Cr contents cause the significant differences in the corrosion rate, which confirmed the accelerated corrosion effect of Mn in the first stage. Along with the disappearance of local Mn agglomerates in the corrosion product, the chemical shift observed from the XPS results presented in Fig. 10 means that the electronic structure of the corrosion products was changed by the presence of the anti-corrosion elements. It can be found from the EPMA results presented in Fig. 8 that the absence of Fe in the local regions occurs because of the high diffusion rate of the Mn cations throughout the corrosion products during stage one, and the less protective character of the Mn oxides is another cause of the high corrosion rate [41]. Then, the outward diffusion of Mn and Fe through the corrosion product can be observed in Figs. 8d-8f. It is considered that the corrosive medium encroaches on the steel matrix, which gradually occurred until the Cr barrier layer formed. This is an effective method for enhancing the corrosion resistance of the medium Mn steel.

An underlying mechanism responsible for the formation of the corrosion products is also summarized in Fig. 11. During the first stage, the dissolved Fe ions are hydrolysed and oxidized into Fe(II) and Fe(III), accompanied by a good electrochemical activity [42]. The corrosion product consists of a large amount of γ-FeOOH, Fe_2O_3 and Fe_3O_4 and the small amount of β-FeOOH and α-FeOOH. Meanwhile, γ-FeOOH can form due to the crystallization of β-FeOOH and be transformed into α-FeOOH/Fe_3O_4 as the corrosion process proceeds [43, 44]. During stage two, as the compact and thick corrosion product forms, the anodic process can be inhibited by the synergetic effect of the anti-corrosion elements and the relatively stable γ-FeOOH and Fe_3O_4 products. From the EMPA results, it can be clearly seen that the Mn element is much more condensed in the corrosion product than that in the matrix. A semiquantitative analysis

was carried out using the XPS results of the main elements. The cationic fraction of the main elements, Fe and Mn, can be calculated by the following equation:

$$C_x = \frac{I_x / S_x}{\sum I_x / S_x} \quad (2)$$

where I_x represents the peak intensity corresponding to the area of the Fe and Mn elements, S_x, which was set as 10.82 for Fe and 9.17 for Mn, represents the relative sensitivity factor.

Because the ionization process did not complete in the corrosion product after 1 day of corrosion testing duration, the calculation results included only the last five corrosion cycles, which are shown in Fig. 12. The cationic fraction in the corrosion product obtained after stage one (before 168 h) shows four times the concentration of the matrix. In addition, the oxidized Fe content increases as the corrosion testing time is prolonged. At stage two, the oxidized Mn content in the corrosion products decreases and stabilizes. The results clearly show the unique role of the pseudo-protective properties achieved with high concentrations of Mn in the initial corrosion stage of the medium Mn steel.

5. CONCLUSIONS

The increase in the manganese and chromium contents in the medium manganese steel changes the corrosion performance of the medium manganese steel in neutral salt spray environments. The new insights of this study are elaborated as follows:

- The increased manganese content in the medium manganese steel obviously impacts the initial corrosion process. β-FeO(OH) appears, especially in environments containing Cl^- ions and when excess Mn exists in the matrix, which causes a direct electrochemical reaction to occur.
- The high protective ability of the corrosion product of the medium Mn steel is related to the decrease in the Mn cationic fraction in the corrosion product and the formation of the anti-corrosion element barrier between the corrosion products and matrix. Moreover, forming a barrier layer containing Cr compounds in the dense corrosion products is an effective method for enhancing the corrosion resistance of the medium Mn steel in a long service situation.
- An obvious valence transformation of the Mn compounds in the corrosion products occurs as the corrosion time is prolonged, while, at the same time, the disappearance of local Mn

agglomerates in the corrosion product caused by the high diffusion rate explains that the adverse effect of Mn is the essential reason for the poor corrosion performance of the medium Mn steel incorporated with low contents of anti-corrosion elements.

ACKNOWLEDGEMENT

This research is supported by the National High Technology Research and Development Program of China (863 Program) No. 2015AA03A501.

References

[1] D.A. Wahab, E. Blanco-Davis, A.K. Ariffin, J. Wang, Ocean Eng. 169 (2018) 125-133
[2] Y. Wang, N. Wang, Mar. Pol. 99 (2019) 42-49
[3] J. Hu, L. Du, G. Sun, H. Xie, R.D.K. Misra, Scripta Mater. 104 (2015) 87-90
[4] E. De Moor, D.K. Matlock, J.G. Speer, M.J. Merwin, Scripta Mater. 64 (2011) 185-188
[5] J. Speer, D.K. Matlock, B.C. De Cooman, J.G. Schroth, Acta Mater. 51 (2003) 2611-2622
[6] S. Fajardo, I. Llorente, J.A. Jiménez, J.M. Bastidas, D.M. Bastidas, Corros. Sci. 154 (2019) 246-253
[7] K.M. Moon, D.A. Kim, Y.H. Kim, Int. J. Modern Phys. B 32 (2018) 1840083
[8] D. Zhang, X. Gao, G. Su, L. Du, Z. Liu, J. Hu, J. Mater. Eng. Perform. 26 (2017) 2599-2607
[9] G. Su, X. Gao, D. Zhang, C. Cui, L. Xiu, C. Yu, J. Hu, Z. Liu, Corrosion 73 (2017), 1367-1380
[10] DIN EN ISO 9227, Corrosion Tests in Artificial Atmospheres-Salt Spray Tests, Deutsches Institut für Normung e.V. (DIN), 2006, pp. 1-24
[11] M. Palm, R. Krieg, Corros. Sci. 64 (2012) 74-81
[12] Y.H. Qian, C.H. Ma, D. Niu, J.J. Xu, M.S. Li, Corros. Sci. 74 (2013) 424-429
[13] D. Raabe, S. Sandlöbes, J. Millán, D. Ponge, H. Assadi, M. Herbig, P.-P. Choi, Acta Mater. 61 (2013) 6132-6152
[14] G. Su, X Gao, T. Yan, D. Zhang, C. Cui, L. Du, Z. Liu, Y. Tang, J. Hu, Mater. Sci. Eng., A 736 (2018) 417-430
[15] M.-M. Wang, C.C. Tasan, D. Ponge, D. Raabe, Acta Mater. 111 (2016) 262-272
[16] B. Sun, R. Ding, N. Brodusch, H. Chen, B. Guo, F. Fazeli, D. Ponge, R. Gauvin, S. Yue, Mater. Sci. Eng., A 749 (2019) 235-240
[17] G. Su, X. Gao, D. Zhang, L. Du, J. Hu, Z. Liu, JOM 70 (2018) 672-679
[18] J. Hu, L.X. Du, H. Liu, G.S. Sun, H. Xie, H.L. Yi, R.D.K. Misra, Mater. Sci. Eng., A 647 (2015) 144-151
[19] ASTM Standard G1-03, Standard practice for preparing, cleaning, and evaluating corrosion test specimens, ASTM, International, West Conshohocken, PA, United States
[20] Z. Liu, X. Gao, J. Li, L. Du, C. Yu, P. Li, X. Bai, Electrochim. Acta 213 (2016) 842-855
[21] J. Yu, H. Wang, Y, Yu, Z. Luo, W. Liu, C. Wang, Corros. Sci. 133 (2018) 276-287
[22] N.K. Tewary, A. Kundu, R. Nandi, J.K. Saha, S.K. Ghosh, Corros. Sci. 113 (2016) 57-63
[23] M. Stipaničev, F. Turcu, L. Esnault, E.W. Schweitzer, R. Kilian, R. Basseguy, Electrochim. Acta 113 (2013) 390-406

[24] J. Alcántara, B. Chico, I. Díaz, D. de la Fuente, M. Morcillo, Corros. Sci. 97 (2015) 74-88
[25] R.A. Antunes, I. Costa, D.L.A. de Faria, Mater. Res. 6 (2003) 403-408
[26] R.A. Antunes, R.U. Ichikawa, L.G. Martinez, I. Costa, Int. J. Corros. (2014) 419570
[27] A. Raman, S. Nasrazadani, L. Sharma, Metallography, 22 (1989) 79-96
[28] A. Raman, S. Nasrazadani, L. Sharma, A. Razvan, Pract. Met. 24 (1987) 577-589
[29] K.J. Gallagher, D.N. Phillips, Trans. Faraday Soc. 64 (1968) 785-795
[30] B.J. Li, H.Q. Cao, J. Shao, M.Z. Qu, Chem. Commun. 47 (2011) 10374-10376
[31] P. Ghods, O.B. Isgor, J.R. Brown, F. Bensebaa, D. Kingston, Appl. Surf. Sci. 257 (2011) 4669-4677
[32] Y.S. Zhang, X.M. Zhu, Corros. Sci. 41 (1999) 1817-1833
[33] T. Yamashita, P. Hayes, Appl. Surf. Sci. 254 (2008) 2441-2449
[34] W. Fredriksson, K. Edström, C.-O. Olsson, Corros. Sci. 52 (2010) 2505-2510
[35] H. Luo, S. Zou, Y.-H. Chen, Z. Li, C. Du, X. Li, Corros, Sci (2019) 108287
[36] Y.Y. Chen, H.J. Tzeng, L.I. Wei, L.H. Wang, J.C. Oung, H.C. Shih, Corros. Sci. 47 (2005) 1001-1021
[37] M. Kimura, H. Kihira, N. Ohta, M. Hashimoto, T. Senuma, Corros. Sci. 47 (2005) 2499-2509
[38] Z.G. Liu, X.H. Gao, C. Yu, L.X. Du, J.P. Li, P.J. Hao, Acta Metall. Sin. (Engl. Lett.) 28 (2015) 739-747
[39] M. Itagaki, R. Nozue, K. Watanabe, H. Katayama, K. Noda, Corros. Sci. 46 (2004) 1301-1310
[40] T. Mizoguchi, Y. Ishii, T. Okada, M. Kimura, H. Kihira, Corros. Sci. 47 (2005) 2477-2491
[41] R. Silva, C. Arana, A.M. de Sousa Malafaia, A.A. Mendes Filho, C. Pascal, J. Otubo, V.L. Sordi, C.A.D. Rovere, Corros. Sci. 158 (2019) 108103
[42] L. Hao, S.X. Zhang, J.H. Dong, W. Ke, Corros. Sci. 54 (2012) 244-250
[43] M. Strarmann, H. Streckel, Corros. Sci. 30 (1990) 697-714
[44] F. Corvo, J. Minotas, J. Delgado, C. Arroyave, Corros. Sci. 47(2005) 883-892

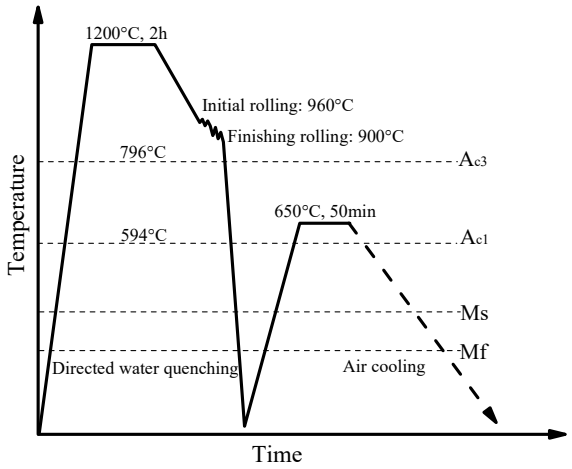

Fig. 1. Schematic diagram of hot rolling and heat treatment process.

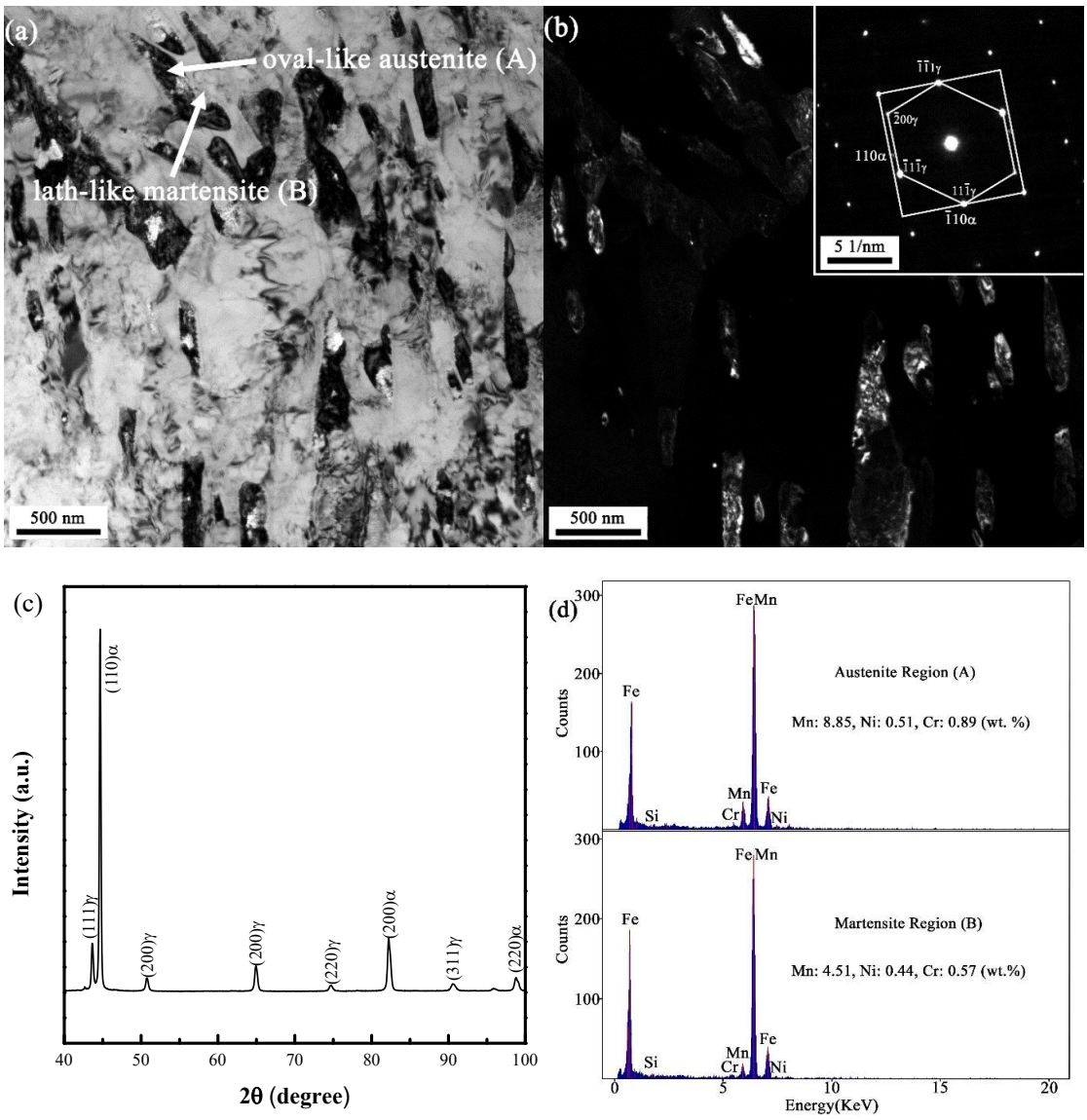

Fig. 2. (a)-(b) TEM micrographs of tested steel tempered at 650 °C for 50 min of bright-field image, dark-field image and SAED pattern of austenite; (c) XRD patterns of tested steel tempered at 650 °C for 50 min; and (d) Representative EDX results.

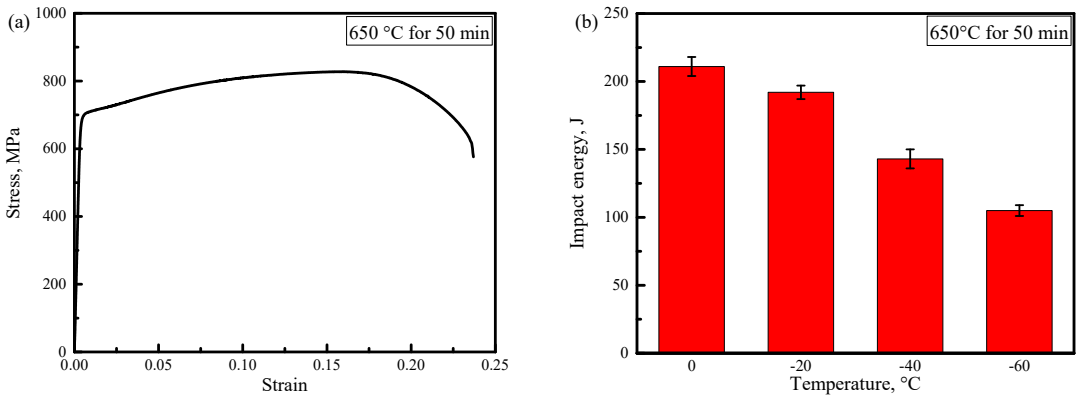

Fig. 3. (a) Engineering stress-strain curve of tested steel; and (b) Charpy impact energy of tested steel at different test temperatures (The length of the error bar in Fig. 2b denotes the standard deviation in three tested coupons).

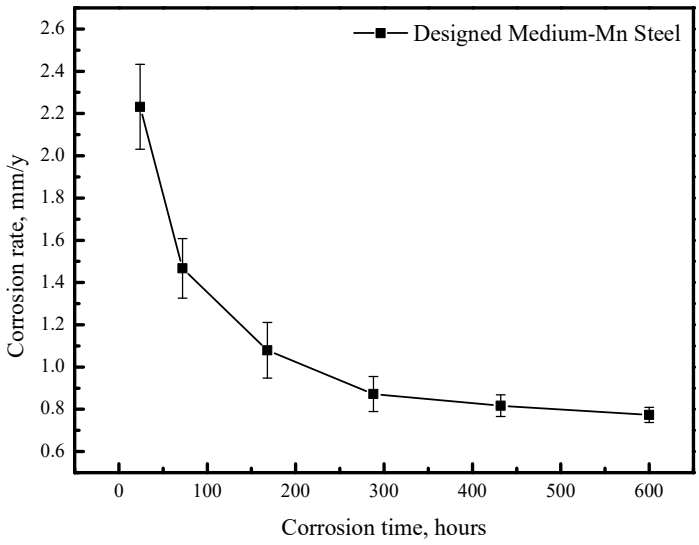

Fig. 4. Corrosion kinetic curve of the tested medium Mn steel in the neutral salt spray condition (The length of the error bar denotes the standard deviation in five tested coupons).

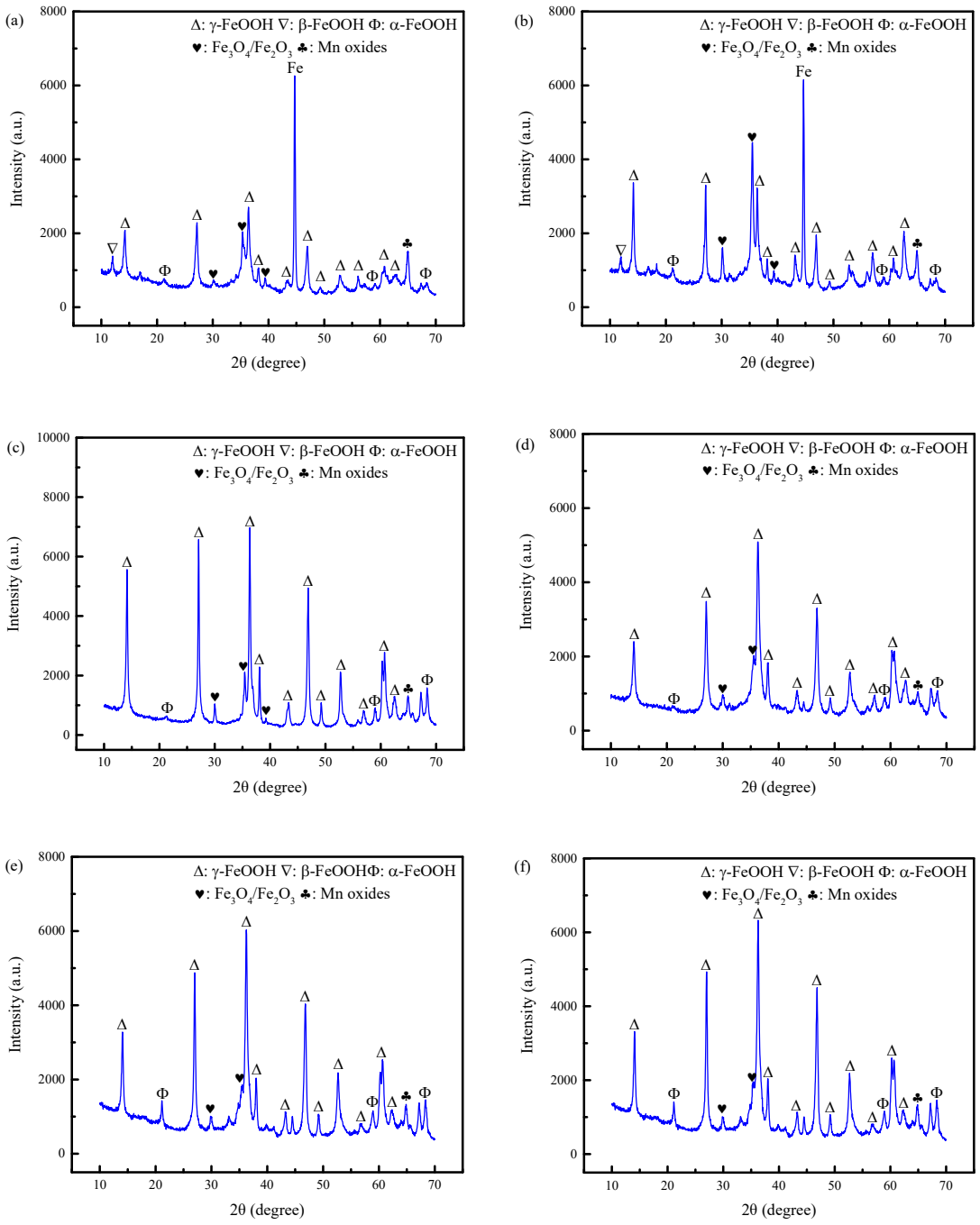

Fig. 5. XRD patterns of surface corrosion products formed after different corrosion durations: (a) 24 h; (b) 72 h; (c) 168 h; (d) 288 h; (e) 432 h; and (f) 600 h.

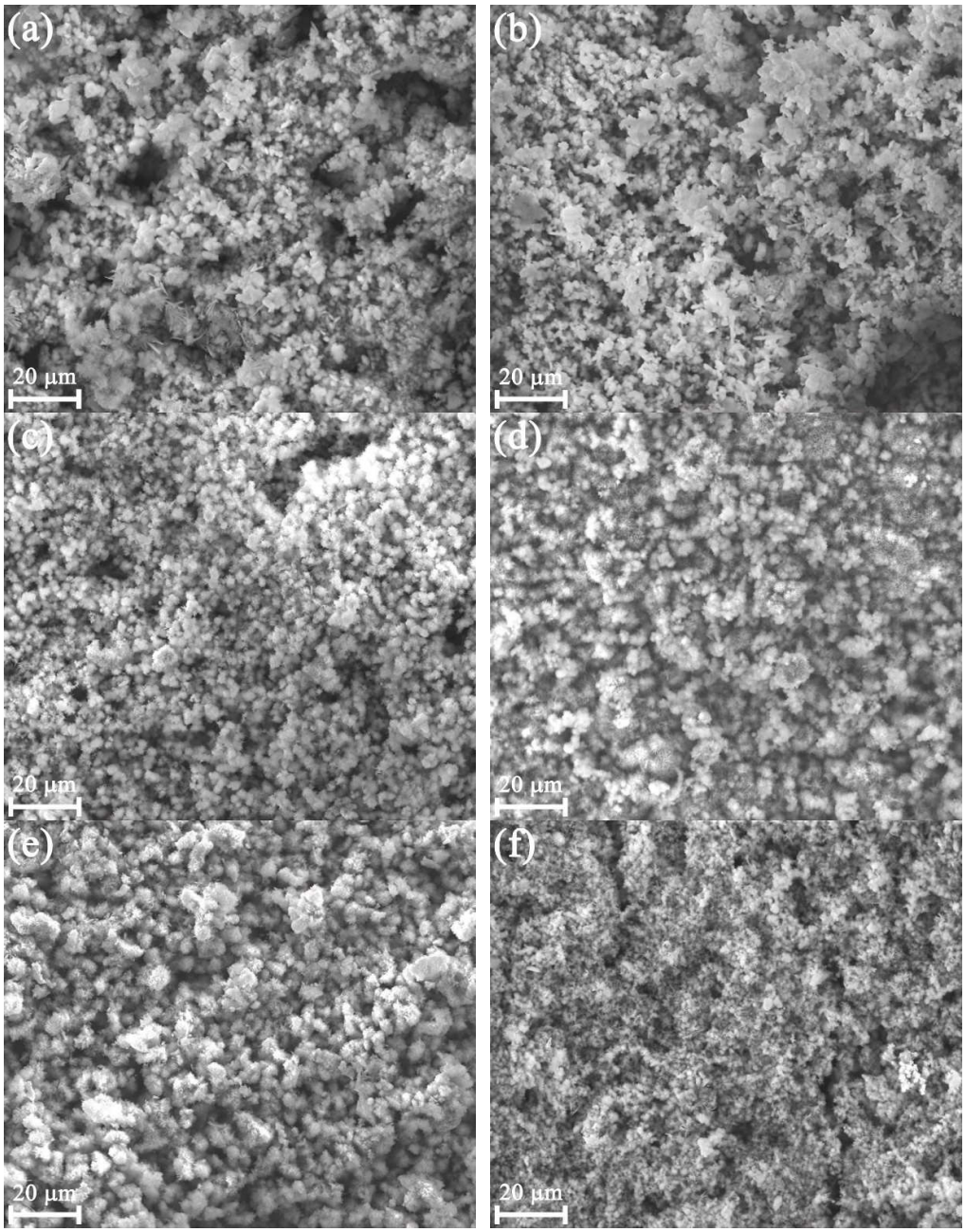

Fig. 6. Surface morphologies of corrosion products formed after different corrosion durations: (a) 24 h; (b) 72 h; (c) 168 h; (d) 288 h; (e) 432 h; and (f) 600 h.

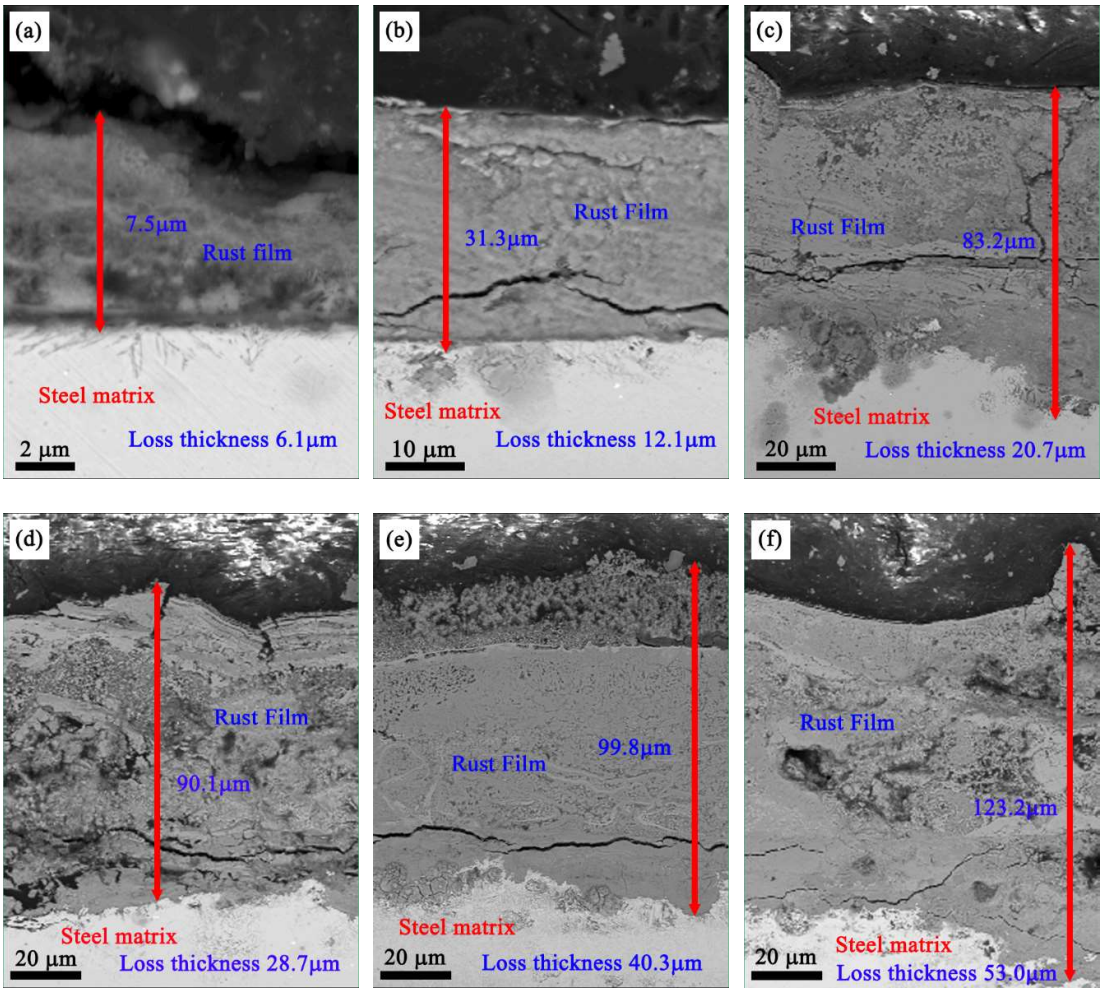

Fig. 7. Cross-sectional morphologies of corrosion products formed after different corrosion durations: (a) 24 h; (b) 72 h; (c) 168 h; (d) 288 h; (e) 432 h; and (f) 600 h.

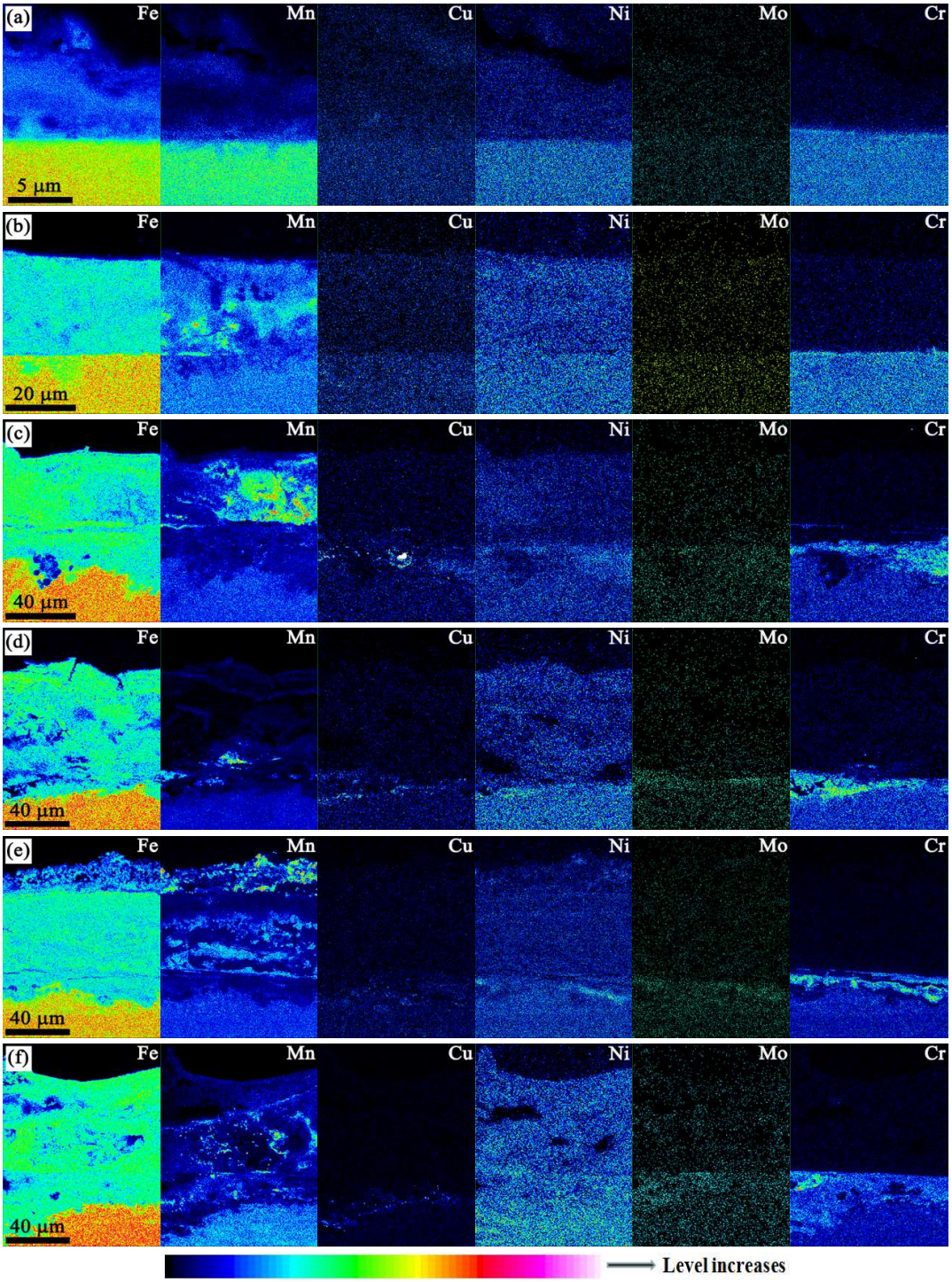

Fig. 8. Elemental distributions of corrosion products formed after different corrosion durations: (a) 24 h; (b) 72 h; (c) 168 h; (d) 288 h; (e) 432 h; and (f) 600 h.

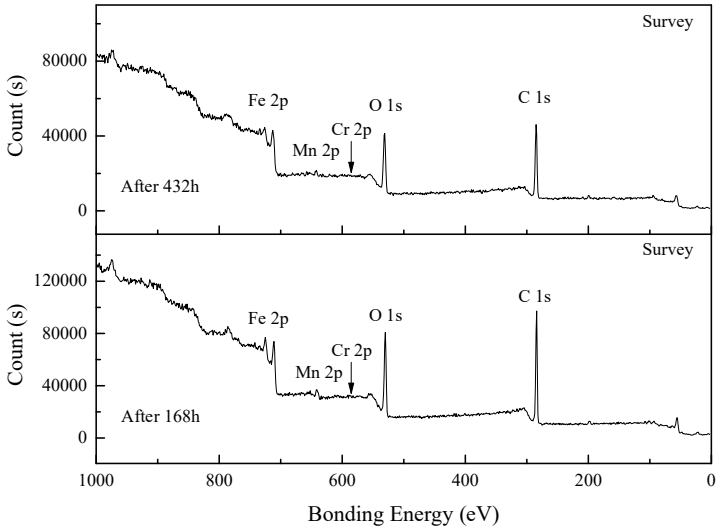

Fig. 9. XPS survey spectrum recorded for the corrosion products formed at the surface of the tested medium Mn steel after corrosion testing times of 168 h and 432 h.

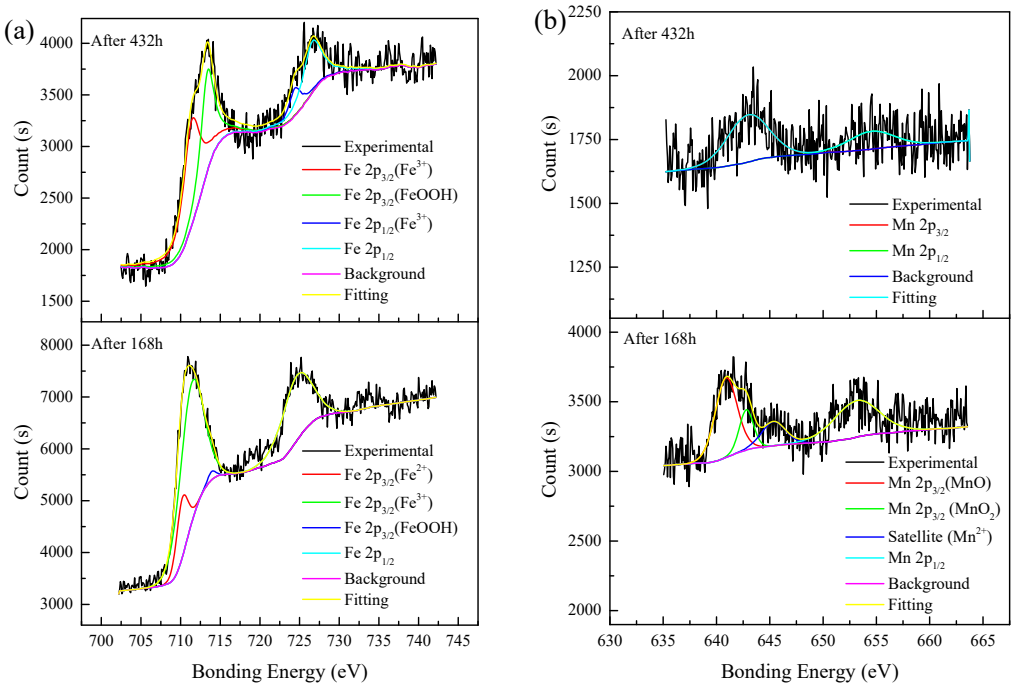

Fig. 10. XPS patterns of corrosion products after corrosion testing times of 168 h and 432 h: (a) Fe 2p; and (b) Mn 2p.

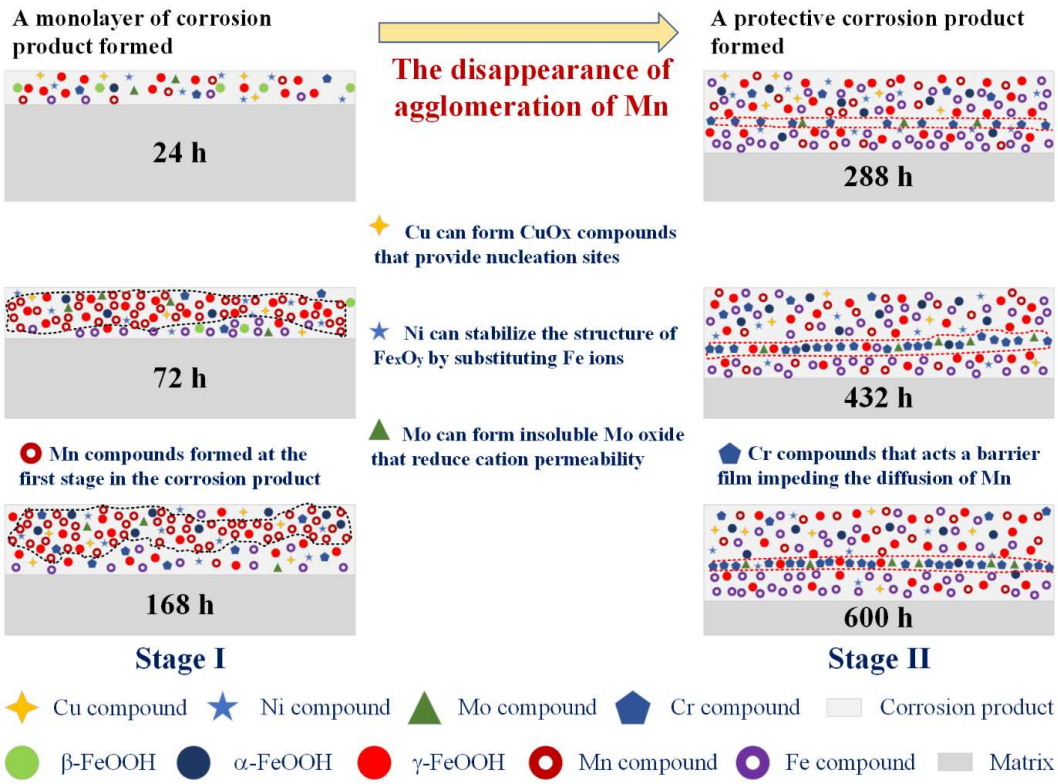

Fig. 11. Schematic sketch showing the roles of alloying elements in the corrosion process of the medium Mn steel exposed to a neutral salt spray environment.

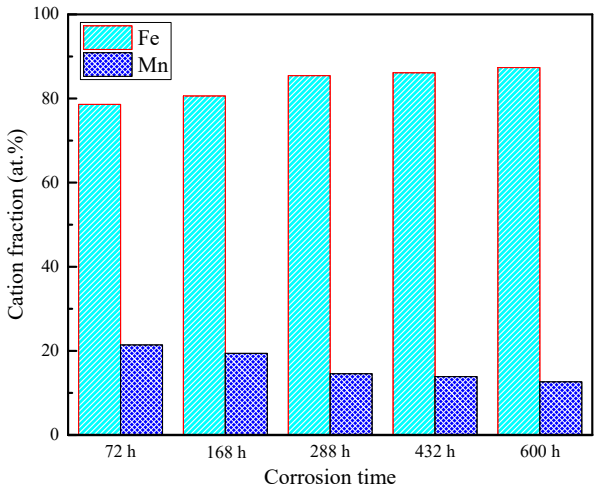

Fig. 12. XPS cationic fraction (C_x) in the corrosion products after different corrosion durations.

Table 1

Chemical composition of designed medium manganese steel (wt %).

Elements	C	Mn	Si	P	S	Al	Cu	Mo	Ni	Cr	Fe
Content	0.05	5.9	0.2	0.006	0.003	0.015	0.3	0.2	0.3	0.8	Bal.